H2/LiF(001) diffractive scattering under fast grazing incidence using a DFT-based potential energy surface

Muzas, A.S.; Cueto, M. del; Gatti, F.; Somers, M.F.; Kroes, G.J.; Martín, F.; Díaz, C.

H_2/LiF(001) diffractive scattering under fast grazing incidence using a DFT-based potential energy surface

A. S. Muzas,[1] M. del Cueto,[1] F. Gatti,[2] M. F. Somers,[3] G. J. Kroes,[3] F. Martín,[1,4,5] and C. Díaz[1,5,6,*]

[1]*Departamento de Química Módulo 13, Universidad Autónoma de Madrid, 28049 Madrid, Spain*

[2]*CTMM, Institut Charles Gerhardt, UMR 5253, Université de Montpellier II, Place Eugène Bataillon, 34095 Montpellier, France*

[3]*Leiden Institute of Chemistry, Gorlaeus Laboratories, Leiden University, P.O. Box 9502, 2300 RA Leiden, The Netherlands*

[4]*Instituto Madrileño de Estudios Avanzados en Nanociencia (IMDEA-Nanociencia), Cantoblanco 28049 Madrid, Spain*

[5]*Condensed Matter Physics Center (IFIMAC), Universidad Autónoma de Madrid, 28049 Madrid, Spain*

[6]*Institute for Advanced Research in Chemical Sciences (IAdChem), Universidad Autónoma de Madrid, 28049 Madrid, Spain*

(Received 26 September 2017; published 27 November 2017)

Grazing incidence fast molecule diffraction (GIFMD) has been recently used to study a number of surfaces, but this experimental effort has not been followed, to present, by a subsequent theoretical endeavor. Aiming at filling this gap, in this work, we have carried out GIFMD simulations for the benchmark system H_2/LiF(001). To perform our study, we have built a six-dimensional potential energy surface (6D-PES) by applying a modified version of the corrugation reducing procedure (CRP) to a set of density functional theory (DFT) energies. Based on this CRP interpolated PES, we have conducted quantum dynamics calculations using both the multiconfiguration time-dependent Hartree and the time-dependent wave packet propagation methods. We have compared the results of our GIFMD simulations with available experimental spectra. From this comparison, we have uncovered a prominent role of the interaction between the quadrupole moment of H_2 and the electric field associated with LiF(001) for specific incidence crystallographic directions. We show that, on the one hand, the molecule's initial rotation strongly affects its diffractive scattering and, on the other hand, the scattering is predominantly rotationally elastic over a wide range of incidence conditions typical for GIFMD experiments.

DOI: 10.1103/PhysRevB.96.205432

I. INTRODUCTION

Grazing (1°–3°) incidence fast (0.2–25 keV) atomic and molecular diffraction, GIFAD and GIFMD techniques, have received quite a lot of attention during the present century. Since 2007, when the first experimental results for LiF(001) [1] and NaCl(001) [2] were published, the number of measurements and systems studied have increased considerably (see [3] and references therein), including a significant amount of studies using molecular projectiles [1,2,4–6]. Spectra measured for molecular projectiles are richer than for atomic projectiles due to the internal molecular degrees of freedom (DOFs) [7], and therefore they are in principle a more sensitive tool for surface analysis. From a theoretical point of view, the diffraction of atomic projectiles has been widely studied [4,6,8–16]. However, little attention has been devoted to molecular projectiles, beyond some classical scattering studies [17–19], although in this case theory can play a key role in understanding experimental results.

To carry out GIFMD simulations, provided that the Born-Oppenheimer static surface (BOSS) approximation holds, two basic steps are required: (i) an accurate description of the electronic structure of the molecule/surface system, i.e., an accurate six-dimensional (6D) potential energy surface (PES), and (ii) a computationally applicable quantum dynamics method. Six-dimensional quantum dynamics has already become a standard tool to study diatomic molecule/surface interactions at low incidence energy(<2 eV), from reactive scattering [20–24] to molecular diffraction [24–26]. However, its accuracy in reproducing experimental data, disregarding phonons and electron-hole pair excitations effects, relies on the accuracy of the underlying potential energy surface (PES) on which the dynamics is carried out [23,27]. Thus the large progress made in the microscopic dynamics description of molecule-surface interaction processes has motivated, subsequently, the development of flexible and accurate methods to determine full-dimensional PESs. These methods are commonly based on interpolation of density functional theory (DFT) energies, computed for a variable number of configurations. Nowadays a handful of such methods is already available in the literature, such as the corrugation reducing procedure (CRP) [28], the modified Shepard (MS) interpolation method [29,30], the neural networks (NN) method [31,32], the permutation invariant polynomial (PIP-NN) method [33], and the reactive force fields (RFF) method [34].

Here our aim is to scrutinize the suitability of the methods developed to study diffractive scattering at thermal or quasithermal energies for GIFMD research. We have chosen H_2/LiF(001) as the benchmark system because, on the one hand, there are GIFMD experimental measurements available in the literature [3,35], and, on the other hand, there is an extensive literature devoted to this system in the low incidence energy regime, which will allow us to further test our simulation tools. In fact, diffraction of H_2 from LiF(001) has been popularly used as a benchmark system to test theoretical models and experimental setups, since the 1930s when Stern *et al.* used it to prove the wave nature of atomic and molecular particles [36,37]. These experimental results were also used to describe for the first time selective adsorption [38]. Later on, experiments on rotationally and diffractionally inelastic scattering showed that H_2 could change its rotational state upon collision with LiF(001) [39]. Rotational polarization [40] and time-of-flight measurements were also performed for

*cristina.diaz@uam.es

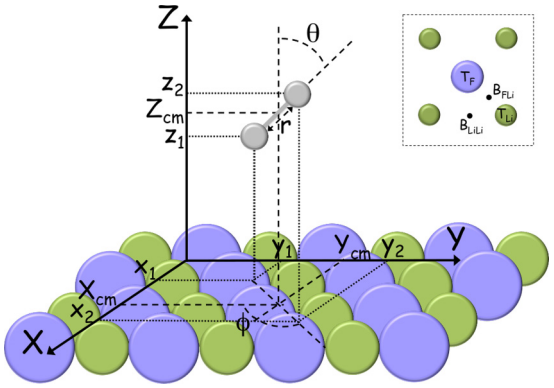

FIG. 1. Cartesian coordinates system. The inset shows the symmetry sites used in the interpolation.

this system [41]. Aiming at understanding these experimental measurements, a number a theoretical models were proposed, although most of them suffered from important shortcomings. Some scattering calculations [42–47] were performed making use of analytical potentials, which do not contain dependence on the H_2 azimuthal angle ϕ (see Fig. 1 for coordinates definition), i.e., potentials that do not allow Δm_J transitions, where m_J is the quantized projection of the rotational angular momentum. Other models [48–52] allow for these transitions, but do not take into account the interaction between the electrostatic field of the surface ions and the quadrupole moment of the H_2 molecule. However, as shown by Hill [53], this interaction plays a key role in H_2/LiF(001) scattering, because it is mainly responsible for rotational transitions. In fact, more recently theoretical simulations [54,55], based on a five-dimensional model (using the rigid rotor approximation), revealed the importance of including the electrostatic interaction in the model and states with different m_J in the basis set for reproducing experimental results showing large differences in the diffraction intensities for para-H_2 ($J = 0$) and normal-H_2 ($J = 0$ and $J = 1$ in the ratio 1:3) [56]. For this system also isotopic effects have been studied [57,58].

To perform our detailed analysis of diffraction of H_2 from LiF(001) under fast grazing incidence, we have built a six-dimensional (6D) potential energy surface (PES) based on density functional theory (DFT) calculations. To build such PES, we have used a modified version of the CRP method, which is described in Sec. II A. Since this is a 6D DFT-based PES generated for an insulating surface, the accuracy of the new interpolation scheme has been carefully checked. Based on this PES, we have carried out dynamics simulations using both the time-dependent wave packet (TDWP) method [21] and the multiconfiguration time-dependent Hartree (MCTDH) method [59]. Our first results using a combination of these methods [60] have revealed that the differences observed experimentally in the diffraction spectra as a function of the incidence direction are mainly due to the interaction between the quadrupole moment of the molecule and the electric field associated with the ionic surface. Here we present an exhaustive study of diffraction as a function of both the internal DOFs of the molecule and the normal incidence energy. Finally, we have also analyzed the probabilities of rotational excitation and deexcitation upon diffraction as a function of the incidence energy and the initial rotational state.

II. METHODOLOGY

To perform our study, we have worked within the BOSS approximation. Here, we should point out that, although experimental results at low incidence energies indicate that 75% of the H_2/LiF(001) interaction should be phonon inelastic [39], recent diffraction experiments on molecule/metal systems [61] suggest that relative intensities of rotational and diffractive transitions are not much affected by phonon. Electron excitations are not expected to play a prominent role in view of the large band gap characterizing LiF. Furthermore, the possibility of performing experiments in which both the angular distribution and the energy loss of the scattered projectiles [62] are measured allows one to separate the contributions of electronic excitations and scattering, thus providing the ideal framework for assessing the results of BOSS theoretical simulations.

Following the BOSS formalism, we have first computed the PES of the system by keeping the surface atoms frozen at their equilibrium position, i.e., by considering only the six DOFs of the molecule (see Fig. 1). In a second step, we have studied the nuclear motion of the molecule, by means of quantum dynamics, on this 6D-PES.

A. H_2/LiF potential energy surface

To carry out dynamics simulations, we need a continuous PES. To compute such a PES for H_2/LiF(001), we have interpolated a dense set of DFT-GGA (generalized gradient approximation) energies applying a modified version of the corrugation reducing procedure (CRP). The DFT-GGA energies have been computed using the plane-wave based code VASP (Vienna ab-initio simulation program) [63,64]. In applying the DFT-GGA method, we have chosen the PW91 functional [65]. The ion cores have been described using the projector augmented wave (PAW) method [66]. We have used a cutoff energy of 800 eV to limit the plane-wave expansion, and a $5 \times 5 \times 1$ k-point grid to sample the Brillouin zone. To model the adsorbate/substrate system, we have used a five-layer slab and a (2×2) surface unit cell. To avoid artifacts caused by the use of periodic boundary conditions in the direction perpendicular to the slab, we have placed a vacuum layer of 20 Å between the slabs in the Z direction. From our converged calculations, we have obtained a lattice constant value equal to 2.88 Å, in good agreement with previous theoretical results [67,68] and with the experimental value of 2.84 Å [69]. The interlayer distance after relaxation was found to be 1.98 Å. The topmost layer presents a rumpling of 0.065 Å, with the F^- ions displaced outwards and the Li^+ ions inwards, in good agreement with previous theoretical calculations [67,70,71].

Using the modified CRP method, the 6D PES can be written as

$$V_{6D}(\mathbf{R}) = I_{6D}(\mathbf{R}) + V_{3D}(\mathbf{r_1})L_{z_0,\delta z}(\mathbf{r_1}) + V_{3D}(\mathbf{r_2})L_{z_0,\delta z}(\mathbf{r_2}), \quad (1)$$

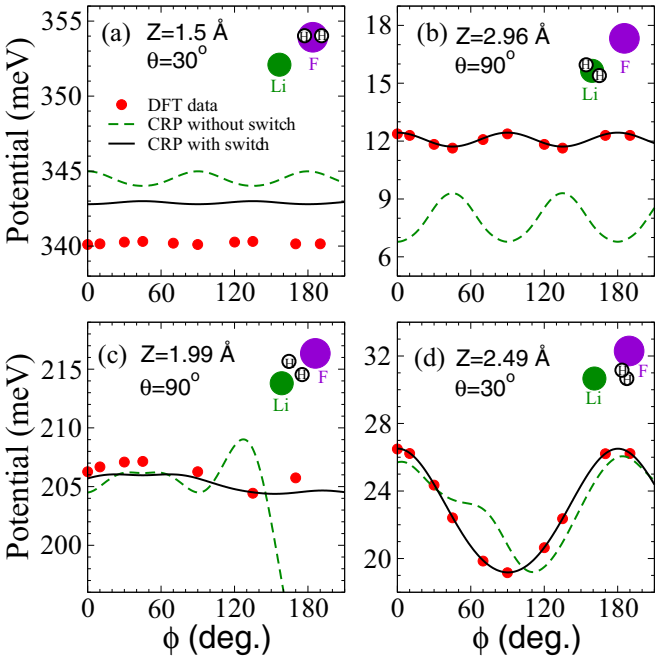

FIG. 2. 1D potential along ϕ. In all the panels $r = 0.80$ Å. The legend with or without switch indicates the use or not of the logistic function with parameters: $z_0 = 1.06$ Å and $\delta z = 0.21$ Å. Panel (d) shows a random (X_{cm}, Y_{cm}) position outside a high symmetry site, $X_{cm} = 0.96$ Å and $Y_{cm} = 0.48$ Å.

where

$$L_{z_0,\delta z}(\mathbf{r_i}) = \left[1 + \left(\exp\left[\frac{z_i - z_0}{\delta z}\right]\right)\right]^{-1}. \quad (2)$$

In Eq. (1), $I_{6D}(\mathbf{R})$ represents a 6D smooth function, where $\mathbf{R}$ stands for the molecular DOFs (see Fig. 1). $V_{3D}(\mathbf{r_i})$ is the atomic repulsive potential, i.e., the interaction between an atom of the molecule and the surface, $\mathbf{r_i}$ being the atomic coordinates (x_i, y_i, z_i). $L_{z_0,\delta z}$ represents a logistic function, which controls the amount of repulsion that is taken into account when computing I_{6D}. The idea of introducing the $L_{z_0,\delta z}$ function comes from the fact that, at long distances from the surface, V_{6D} is already smooth enough to be interpolated directly, without subtracting any repulsive term. The choice of the z_0 and δz parameters controls the *amount of CRP* applied to the interpolation. At long distances, we have found that a complete CRP interpolation introduces numerical noise in I_{6D}. Thus the addition of the logistic function ensures a more stable interpolation when the distance to the surface becomes long enough. The numerical noise avoided in this way would otherwise not only lead to spurious fluctuations in the potential, it could also lead to erroneous symmetries with respect to rotations in θ and ϕ. Some representative examples of this problem are shown in Fig. 2, where we have displayed the potential as a function of the azimuthal angle (ϕ) for several configurations $(X_{cm}, Y_{cm}, Z_{cm}, r, \theta)$. From this figure, we can see that the PES interpolated with the modified CRP yields more accurate results, in comparison with DFT data not used in the interpolation, than the PES interpolated with the standard CRP method.

TABLE I. (Z, r, θ, ϕ) molecular configurations used in the interpolation process. T=top and B=bridge. (*See inset Fig. 1.)

Site*	$(\theta,\phi)_1$	$(\theta,\phi)_2$	$(\theta,\phi)_3$	$(\theta,\phi)_4$	$(\theta,\phi)_5$	$(\theta,\phi)_6$	$(\theta,\phi)_7$
T Li	(0,0)	$(\frac{\pi}{4},0)$	$(\frac{\pi}{2},0)$	$(\frac{\pi}{4},\frac{\pi}{4})$	$(\frac{\pi}{2},\frac{\pi}{4})$		
T F	(0,0)	$(\frac{\pi}{4},0)$	$(\frac{\pi}{2},0)$	$(\frac{\pi}{4},\frac{\pi}{4})$	$(\frac{\pi}{2},\frac{\pi}{4})$		
B LiLi	(0,0)	$(\frac{\pi}{2},0)$	$(\frac{\pi}{2},\frac{\pi}{4})$	$(\frac{\pi}{2},\frac{\pi}{2})$			
B LiF	(0,0)	$(\frac{\pi}{2},0)$	$(\frac{\pi}{2},\frac{3\pi}{10})$	$(\frac{\pi}{2},\frac{4\pi}{5})$	$(\frac{3\pi}{4},0)$	$(\frac{3\pi}{4},\frac{3\pi}{10})$	$(\frac{3\pi}{4},\frac{4\pi}{5})$

To perform the interpolation, we have used 4116 DFT single point energies, which are grouped in 21 $(X_{cm}, Y_{cm}, \theta, \phi)$ configurations (see Table I). For each configuration, we have computed 196 DFT single point energy values by varying Z_{cm} from 0.25 to 7.0 Å and r from 0.4 to 2.3 Å. To evaluate I_{6D}, we first carry out a cubic spline interpolation of each of the 2D cuts (Z_{cm}, r) of the grid, and then a symmetry adapted Fourier interpolation is performed along θ and ϕ for each high symmetry site. This procedure allows one not only to define I_{6D} at each high symmetry site, but also to define its first derivatives. Finally, in order to get I_{6D} and its derivatives for any geometry, a Fourier interpolation is performed in (X_{cm}, Y_{cm}) and ϕ based on the previous ones. Details about the interpolation of the V_{3D} potentials are given in Ref. [14].

In Fig. 3, we show several 2D (r, Z_{cm}) cuts corresponding to the 6D interpolated potential. From this figure, we can see that the Li top sites present the higher anisotropy, whereas the lower anisotropy is found for the Li-F bridge sites. We can also observe that, as it could be anticipated, helicopter ($\theta = 90°$) configurations are energetically more stable than cartwheel configurations over the Li sites, because the positive charge located on the Li ion interacts favorably with the excess of negative charge located in the H_2 bond, whereas the opposite holds over the F sites.

B. Dynamics

Within the BOSS approximation, the Hamiltonian describing our system can be written (in atomic units) as

$$\hat{H} = -\frac{1}{2M}\left[\frac{\partial^2}{\partial X^2} + \frac{\partial^2}{\partial Y^2} + \frac{\partial^2}{\partial Z^2}\right] - \frac{1}{2\mu}\frac{\partial^2}{\partial r^2} + \frac{\hat{J}}{2\mu r^2} + V_{6D}. \quad (3)$$

In this equation, M and μ are the total and the reduced mass of H_2, respectively, and $\hat{J}$ is the rotation operator, of which the eigenfunctions are the spherical harmonics $Y_{Jm_J}(\theta,\phi)$. To study diffractive scattering of H_2 from LiF(001) using this Hamiltonian, we have to solve the time-dependent Schrödinger equation,

$$\hat{H}\,\Phi(\mathbf{R},\mathbf{r};t) = i\frac{\partial\Phi(\mathbf{R},\mathbf{r};t)}{\partial t}. \quad (4)$$

To do so, we have used two different quantum dynamics methods, the TDWP [21,22,72] and the MCTDH [59,73] methods. In this section, we summarize briefly the main characteristics of both methods. A more detailed description can be found in Refs. [21,22,59,73].

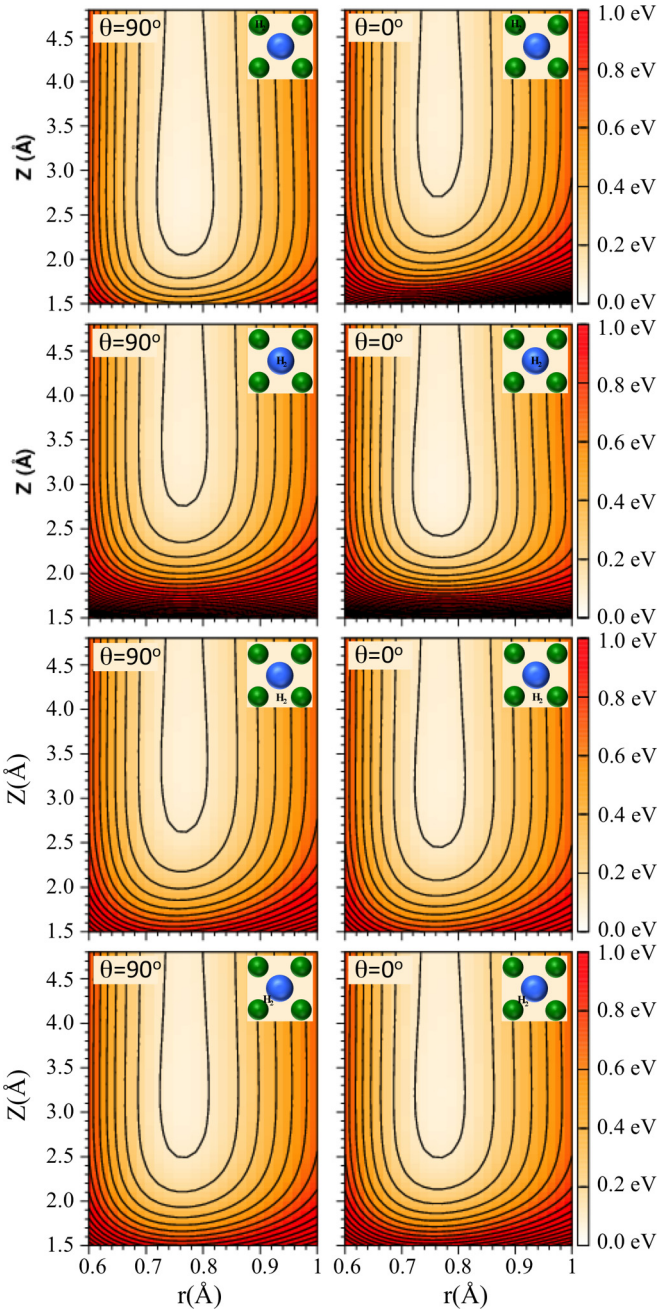

FIG. 3. 2D cuts through the H_2/LiF(001). Left side panels: helicopter configurations; right side panels: cartwheel configurations. From top to bottom: top Li, top F, Li-Li bridge, and Li-F bridge sites. The spacing between the contour levels is 0.1 eV.

1. Time-dependent wave packet propagation (TDWP) method

Within the TDWP framework [21], the dependence of the wave function on X_{cm}, Y_{cm}, Z_{cm}, and r is represented using a direct product discrete variable representation (DVR) [74] with constant grid spacing, and on the angular DOFs using a nondirect product finite basis representation (FBR) of spherical harmonics. To transform the wave function from the angular FBR to the corresponding DVR, and vice versa, Gauss-associated-Legendre and Fourier transforms are used [75].

The TDWP method can be divided in three main steps.

TABLE II. Input parameters used in the TDWP calculations. A detailed description of the parameter can be found in Ref. [80]. The values are in atomic units unless otherwise indicated. S.N.I.= slow normal incidence; F.G.I.=fast grazing incidence.

Parameter	S.N.I.	F.G.I.
Initial wave packet		
Perpendicular energy range (eV)	0.05–0.15	0.15–0.45
Parallel energy (eV)	0.0	199.7
Initial position, Z_0	17.75	18.0
Width, ΔZ_0	0.452	1.357
Grid parameters		
Z minimum value	2.0	1.5
Grid points, N_Z	128	224
Specular grid points, N_Z^{sp}	256	480
Grid spacing, ΔZ	0.15	0.1
r minimum value	0.8	0.7
Grid points, N_r	40	60
Grid spacing, Δr	0.15	0.2
Grid points, N_X (N_Y)	10 (10)	24 (24)
Maximum J in rotational basis	12	14
Time propagation		
Time step, Δt	5	2
Total propagation time	35000	24000–28000
Optical potential in Z (r)		
Initial value, $Z_{\min}$	13.25 (3.65)	13.50 (3.65)
Proportionality constant	0.0055 (0.0099)	0.0058 (0.0191)
Range, L_0	7.80 (3.00)	10.30 (2.85)
Other parameters		
Analysis value, Z_∞	13.25	13.50

(i) The initial wave function (placed in the noninteraction region, Z_∞) is written as the product of a Gaussian wave packet, describing the perpendicular motion to the surface, a plane wave function, describing the parallel translational motion, and a rovibrational wave function, describing the internal initial state of the molecule,

$$\Psi_0(X_{cm},Y_{cm},Z_{cm},r,\theta,\phi) = \varphi_{v,J}(r)Y_{J,m_J}(\theta,\phi) \times \frac{1}{\sqrt{A}} e^{i\mathbf{K_0}\mathbf{R}} \int dk_Z b(k_Z) \frac{1}{\sqrt{2\pi}} e^{ik_Z Z}, \quad (5)$$

where $\varphi_{v,J}(r)$ and $Y_{J,m_J}(\theta,\phi)$ are the vibrational and rotational eigenfunctions, respectively, $\mathbf{K_0}$ the initial parallel momentum vector, $\mathbf{R}$ the position vector (X_{cm},Y_{cm}), and A the unit cell area.

(ii) This initial wave function is propagated using the split operator method [76], in which the kinetic ($\hat{K}$) and potential ($\hat{V}$) propagation parts of the Hamiltonian are symmetrically split as

$$e^{(-i\hat{H}\Delta t)} = e^{-i\hat{K}\frac{\Delta t}{2}} e^{-i\hat{V}\Delta t} e^{-i\hat{K}\cdot\frac{\Delta t}{2}}. \quad (6)$$

Note that by symmetrizing the splitting, the error of this method is of the order of Δt^3.

(iii) Eventually, the backscattering wave function is analyzed at the point beyond which the molecule and the surface no longer interact (Z_∞). The analysis is carried out using the Balint-Kurti formalism [77–79].

In Table II, we summarize the relevant parameters used in our TDWP calculations.

TABLE III. Relevant input parameters used in the MCTDH calculations.

Parameter	S.N.I.	F. G. I.
Initial wave packet		
Perpendicular energy range (eV)	0.084–0.118	0.27–0.33
Parallel energy (eV)	0.0	15.18
Initial position (Å)	7.5	9.0
Width, ΔZ_0 (Å)	0.6	0.6
Primitive grid parameters		
Type X, Y, Z	FFT	Same
N_X, N_Y, N_Z	20,20,100	100,100,100
X,Y range (Å)	[0.0,2.88]	Same
Z range (Å)	[0.25,12.0]	Same
Type r	rHO-DVR	
N_r	40	
r range (Å)	0.1–3.96	
Type θ, ϕ	2D Legendre DVR	Same
N_θ, N_ϕ	20,17	Same
Wave representation		
SPFs per (X,Y), (Z,r), (θ,ϕ)	25, 14, 18	Same
Propagation		
Propagation time (fs)	2540	1000
Complex absorbing potential		
Z range (Å)	7.5–12.0	7.5–12.0
Strength, η_Z (a.u.)	1×10^{-4}	2×10^{-4}
r range (Å)	2.24–3.96	
Strength, η_r (a.u.)	1.5×10^{-3}	

2. *Multiconfiguration time-dependent Hartree (MCTDH) method*

Within the MCTDH framework [73], the time-dependent wave function of our system is represented as a sum of time-dependent single-particle functions (SPFs). These SPFs depend on both spatial coordinates and time. Thus

$$\Phi(Q_1,\ldots,Q_f;t)=\sum_{j_1=1}^{n_1}\cdots\sum_{j_f=1}^{n_f}A_{j_1\ldots j_f}(t)\prod_{k=1}^{f}\phi_{j_k}^{(k)}(Q_k;t), \tag{7}$$

where f denotes the number of DOFs, Q_i the ith nuclear coordinate, $A_{j_1\ldots j_f}$ the expansion coefficients, and $\phi_{j_k}^{(k)}$ are the SPFs for each DOF. They are expanded in a time-independent basis set, such as

$$\phi_{j_k}^{(k)}(Q_k;t)=\sum_{i_k=1}^{N_k}a_{i_k,j_k}(t)\zeta_{i_k}^{(k)}(Q_k). \tag{8}$$

The characteristics of the $\zeta_{i_k}^{(k)}(Q_k)$ functions chosen for each DOF are given in Table III.

Here, we have used a scheme in which the modes (X_{cm},Y_{cm}), (r,Z_{cm}), and (θ,ϕ) are combined. Thus our wave function is written as

$$\Phi^{6D}=\sum_{h=1}^{N_{xy}}\sum_{k=1}^{N_{zr}}\sum_{l=1}^{N_{\theta\phi}}A_{hkl}(t)\times\phi_h^{(xy)}(x,y;t)\phi_k^{(zr)}(z,r;t)\phi_l^{(\theta\phi)}(\theta,\phi;t). \tag{9}$$

TABLE IV. Parameters used to represent the H_2/LiF(001) PES in a suitable form for the MCTDH equations of motion using the POTFIT algorithm. Δrms^w and Δrms^{rw} represent the root mean square error on all grid points and on relevant grid points, respectively. max (ϵ) and max (ϵ^r) represent the maximum error on all grid points and on relevant grid points, respectively. ($^{(*)}$ In the case of 5D simulations, only N_Z.)

POTFIT parameters	V_{6D}^{approx}	V_{5D}^{approx}
Natural potential basis		
N_X, N_Y	Contr. [59]	Contr. [59]
N_Z, $N_r^{(*)}$	50	17
N_θ, N_ϕ	253	253
Relevant region of the fit		
Z range (Å)	>0.5	>0.5
r range (Å)	[0.76,4.0]	
V (eV)	<5	<5
Accuracy		
N_{iter}	5	5
Δrms^{rw}, Δrms^w (meV)	2.65,27.72	0.04,2.1
max (ϵ^r), max (ϵ) (meV)	346,1870	1.3,162

In the case of the 5D simulation (rigid rotor model), $\phi_k^{(zr)}(z,r;t)$ becomes $\phi_k^{(z)}(z;t)$. The MCTDH calculations have been performed using the Heidelberg package [81].

Finally, we should point out that, although, in principle, we should perform MCDTH dynamics using exactly the same PES as in the TDWP calculations (described in Sec. II A), from a computational point of view, the MCTDH algorithm is more efficient when combined with a PES that is also expressed as a sum of products of one- or two-dimensional functions [59,73]. To solve this paradox, we have made use of the POTFIT procedure [82,83] to transform our nonseparable potential into a combination of products of 1D and 2D functions. Within the POTFIT algorithm a multidimensional nonseparable PES can be approximated by

$$V^{\text{approx}}\approx\sum_{j_i=1}^{m_1}\cdots\sum_{j_f=1}^{m_f}C_{j_i\ldots j_f}v_{j_i}^{(1)}\big(Q_{i_1}^{(1)}\big)\ldots v_{j_f}^{(f)}\big(Q_{i_f}^{(f)}\big), \tag{10}$$

where the expansion coefficients C_j are obtained by the overlaps between the potential, V, and the natural potentials, v,

$$C_{j_i\ldots j_f}=\sum_{i_1=1}^{N_1}\cdots\sum_{i_f=1}^{N_f}V_{i_1\ldots i_f}v_{i_1j_1}^{(1)}\ldots v_{i_fj_f}^{(f)}. \tag{11}$$

The natural potentials are the orthogonal eigenvectors of the symmetric positive semidefinite potential energy density matrices $\rho^{(k)}$, given by

$$\rho_{ji}^{(k)}=\sum_{i_1=1}^{N_1}\cdots\sum_{i_{k-1}=1}^{N_{k-1}}\sum_{i_{k+1}=1}^{N_{k+1}}\cdots\sum_{i_f}^{N_f}\times V_{i_1\ldots i_{k-1}ji_{k+1}\ldots i_f}V_{i_1\ldots i_{k-1}li_{k+1}\ldots i_f}. \tag{12}$$

In Table IV, we give the relevant parameters related to the POTFIT procedure.

III. RESULTS and DISCUSSION

We have first performed some simulations at quasithermal energies under normal incidence conditions. A comparison between our results and previous ones [55] already gives us some useful information that will be valuable to analyze the GIFMD results. In a second step, we have performed GIFMD simulations.

A. Slow normal incidence

To assess the accuracy of our DFT-based PES, we have first computed rotational deexcitation and diffraction probabilities under slow normal incidence conditions, and we have compared our results with those from Ref. [55]. Results presented in Ref. [55] were obtained using a 5D TWDP method, excluding molecular vibration, and an analytical PES [54,84] that include the expression for the electrostatic ionic lattice–molecular quadrupole moment interaction proposed by Hill [53]. Therefore, this PES includes empirically all the interactions that play a role in the H_2/LiF(001) system, namely, the short range repulsion between closed-shell species, the attractive induced dipole–induced dipole interactions, the induced dipole–induced quadrupole interaction, the electrostatic quadrupole–ionic lattice interaction, and the ionic lattice–induced dipole interaction. In Figs. 4 and 5, we show the comparison between our 6D quantum dynamics calculations and those from Ref. [55]. In Fig. 5, the diffraction probabilities include all m_J contributions. From theses figures, we can extract several interesting conclusions: (i) the agreement between 5D and 6D quantum MCTDH dynamics results (see insets in Figs. 4 and 5) is almost perfect, proving that the rigid solid approximation, already used in Refs. [55,58], can be safely used to study this system; (ii) 6D MCTDH results are in very good agreement with those obtained with the 6D TDWP method, i.e., both methods are equally suitable to study this kind of phenomenon. The advantage of the MCTDH method lies in the fact that it can be straightforwardly used for any number of dimensions. (iii) we have found good agreement between our results and those of Ref. [55]. From this agreement, we can conclude that our DFT-based PES includes all the relevant effects that explain the interaction of a diatomic molecule with an ionic surface, and notably the electrostatic interaction of the H_2 quadrupole moment with the electric field of the ion lattice ($V_{\rm els}$), which, as discussed in Sec. III B, plays a prominent role in explaining diffraction as a function of the crystallographic direction.

B. Fast grazing incidence

In GIFMD, a highly energetic molecule approaches the surface following a trajectory almost parallel to the surface. In this case, only diffraction peaks perpendicular to the crystallographic incidence direction, in the reciprocal lattice (see inset in Fig. 6), can be observed [1,2,85]. In Fig. 7, we show a comparison between typical experimental diffraction spectra [35], measured along the [100] and the [110] direction, and our theoretical simulations, for the initial rotational states $J = 0$ and 3. At this point, it is worth noticing that our theoretical patterns include both rotational elastic and inelastic contributions, although, as discussed below, inelastic

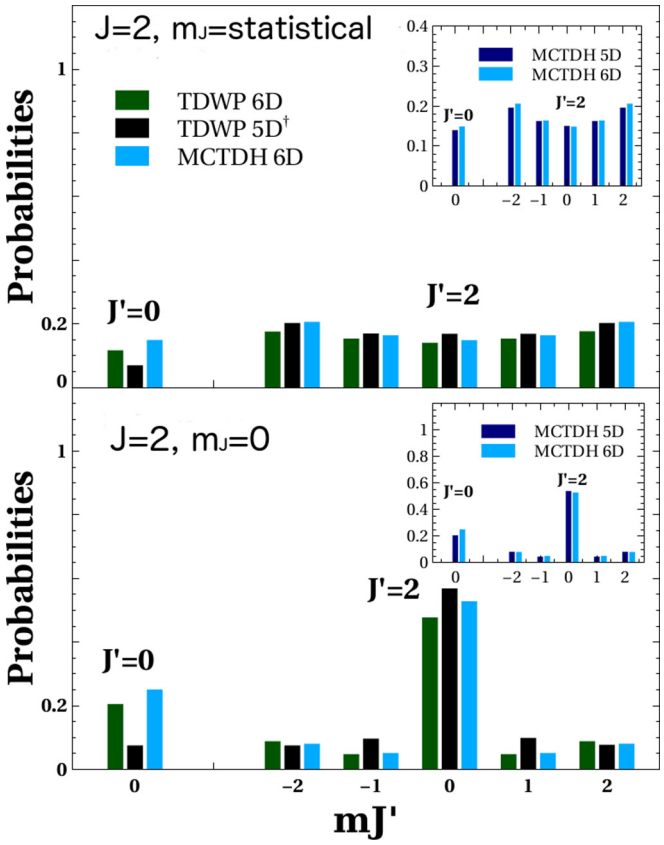

FIG. 4. Rotational deexcitation probabilities at slow normal incidence conditions, $E_n = 0.1$ eV. Top panel: initial rotational state $J = 2$ and statistical distribution of m_J; bottom panel: initial rotational state $J = 2$ and $m_J = 0$. †TDWP 5D results have been taken from Ref. [55]. The inset shows the comparison between 6D and 5D MCTDH results.

contributions are rather small. A swift comparison between these spectra already shows that, although they have been recorded for similar normal energies (∼300 eV), they look very different. In fact, as discussed in Ref. [35], if one uses a simple hard-wall model to extract surface parameters from this spectra, for example, the corrugation, one may find a strikingly large difference depending on the crystallographic direction analyzed, 0.068 Å along the ⟨100⟩ direction versus 0.25 Å along the ⟨110⟩ direction. This result supports the idea that to extract accurate surface parameters, a detailed analysis using accurate theoretical methods is required.

We have performed both 5D-MCTDH and 6D-TDWP calculations for molecules incident in their ground rotational state. In the case of the MCTDH calculations, we have taken advantage of our previous analysis for slow normal incidence, which shows a very good agreement between 5D and 6D-MCTDH calculations (see insets in Figs. 4 and 5). The reduction of the dimensionality has allowed us to simulate GIFMD experiments efficiently with MCTDH, because the computational cost of this method, in its actual implementation, increases considerably when dealing with molecules with large momentum. Also, to reduce the computational cost, we have performed MCTDH calculations using a θ_i value higher than the one used in the experiments, while keeping the

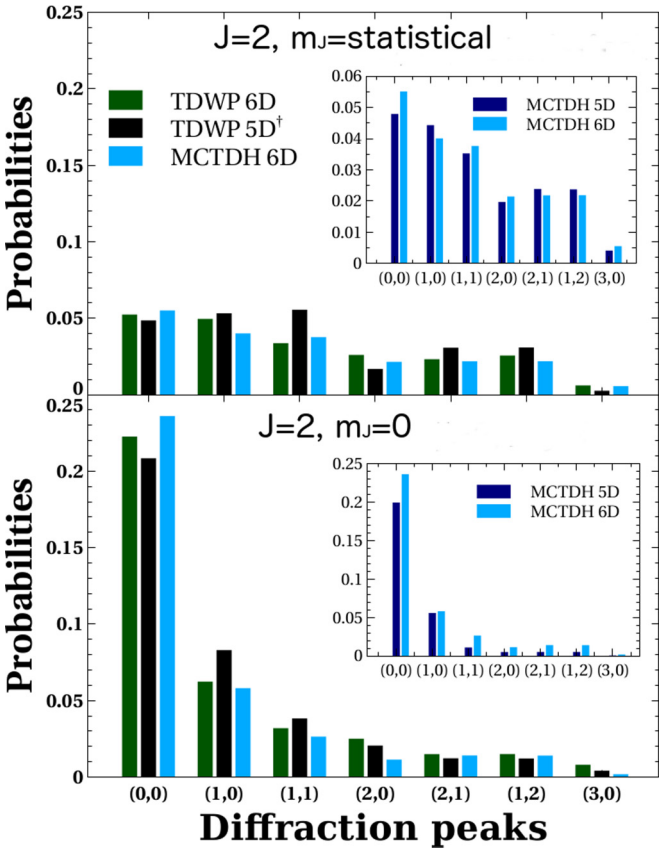

FIG. 5. Diffraction probabilities at slow normal incidence conditions, $E_n = 0.1$ eV. The peak probabilities have been obtained by summing over all final m_J probabilities. Top panel: initial rotational state $J = 2$ and statistical distribution of m_J; bottom panel: initial rotational state $J = 2$ and $m_J = 0$. †TDWP 5D results have been taken from Ref. [55]. The inset shows the comparison between 6D and 5D MCTDH results.

experimental normal energy. We have used $\theta_i = 8°$, whereas typical experimental polar angles are around 1°. In Fig. 7, we compare the experimental spectra with those obtained from 6D-TDWP calculations and the 5D-MCTDH simulations just described (see insets in Fig. 7). In the case of the

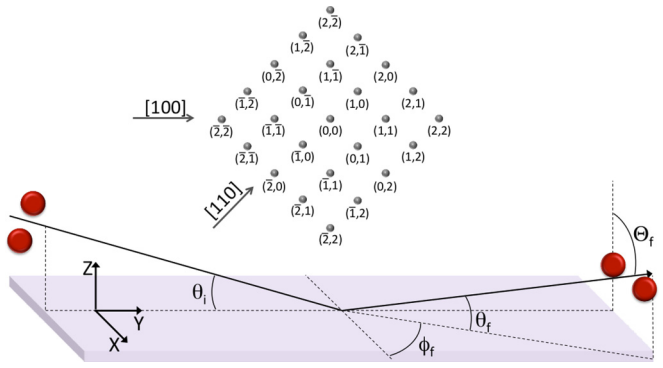

FIG. 6. Schematic representation of a grazing incidence collision of H_2 with LiF(001). The coordinate system used in the dynamics is also shown. The inset shows the reciprocal lattice corresponding to LiF(001).

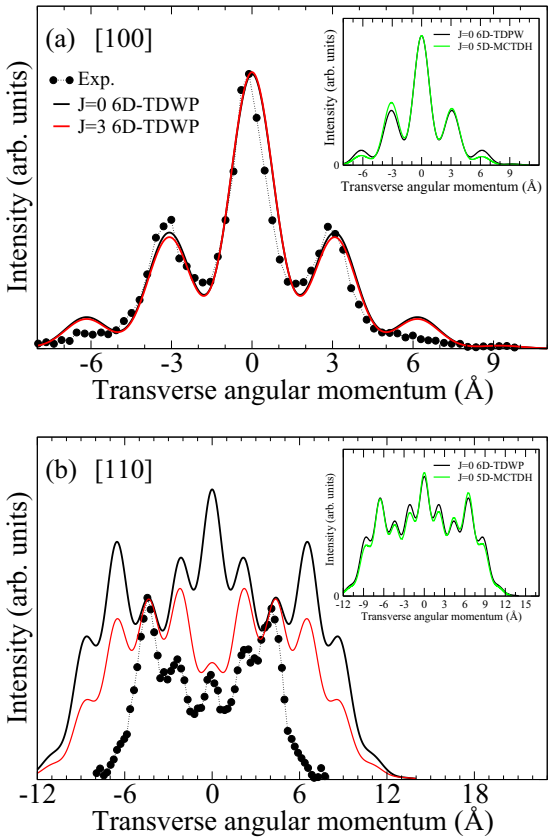

FIG. 7. Experimental and theoretical simulated spectra for H_2 diffracted from LiF(001) for incidence along the [100] (a) and the [110] (b) crystallographic directions, with $E_n = 300$ meV and $\theta_i = 8°$, 2.2°, and 1° for MCTDH, TDWP, and experiment, respectively. Theoretical simulations correspond to H_2 molecules with $(J_i = 0, v_i = 0)$ and $(J_i = 3, v_i = 0)$. Experimental results have been taken from Ref. [35]. To take into account the experimental resolution our theoretical results have been convoluted by using a Gaussian function with $\sigma = 0.8 \text{Å}^{-1}$ (FWHM $= 1.88$ Å^{-1}). For the sake of comparison, the experimental spectra have been normalized to the 6D-TDWP theoretical specular peak in panel (a), and to one of the second order peaks in panel (b).

[100] crystallographic direction [Fig. 7(a)], the agreement between theory and experiment is remarkable, supporting the accuracy of our DFT-based 6D PES. The good agreement between the MCTDH simulations, the TDWP ones, and the experimental results further support our previous conclusions for H/LiF(001) [16], according to which fast grazing incidence conditions are reached for θ_i values higher (E_i lower) than the typical ones used in experiments. On the other hand, for incidence along the [110] direction, although the agreement between 5D-MCTDH and 6D-TDWP simulations is once again excellent, the comparison between experiment and theory is rather poor.

Beyond differences in the extension of the transverse momentum spectrum observed between theory and experiment, that can be mostly attributed to limitations of the experimental setup, the disagreement between 6D-TDWP simulations and experimental measurement along the [110] direction has been the subject of a recent detailed study [60], which has shown

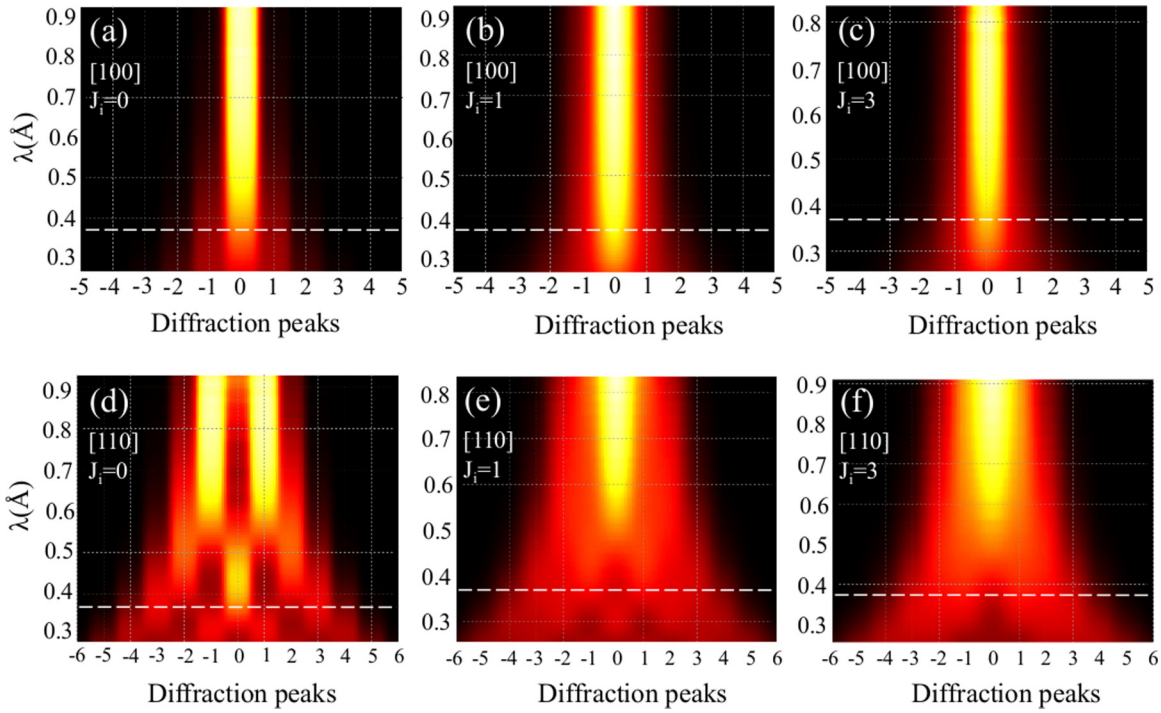

FIG. 8. 6D-DTWP theoretical simulated spectra for H_2 diffracted from LiF(001) as a function of the wavelength for motion normal to the surface. To take into account the experimental resolution our theoretical results have been convoluted by using a 2D Gaussian function with $\sigma_x = 0.4$ and $\sigma_y = 0.01$. The white dashed line indicates the wavelength associated to H_2 at 300 meV, the 1D cuts of which are shown in Fig. 7.

that the internal DOFs of the molecule play a prominent role in this case, contrary to diffraction along the [100] direction, where the effect of the internal DOFs is negligible. The origin of this different behavior is the interaction of the quadrupole moment of the molecule with the electric field associated with the ionic crystal ($V_{\rm els}$). According to previous work by Hill [53]

$$V_{\rm els} = \sum_{n,m} A_{n,m}(\theta,\phi)[1-(-1)^{n+m}], \tag{13}$$

where n and m are the diffraction indices (see inset in Fig. 6), and $A_{n,m}(\theta,\phi)$ a coefficient that depends on the molecule orientation and is expressed in second order spherical harmonics. Perpendicular to the [100] direction, $n+m$ is always even ($V_{\rm els}=0$), whereas perpendicular to the [110] direction $n+m$ is even and odd alternatively. Therefore, the influence of $V_{\rm els}$ is only present along the [110] direction. From Fig. 7, we observe that indeed the simulated spectra essentially do not depend on the initial rotational state along the [100] direction, whereas they strongly depend on J_i along the [110] direction. Furthermore, along this latter direction only molecules with $J_i > 0$ are significantly influenced by $V_{\rm els}$, because for $J_i = 0$ all orientations are equally possible, so that $\langle Y_{00}(\theta,\phi)|A_{n,m}(\theta,\phi)|Y_{00}(\theta,\phi)\rangle = 0$. In fact, as shown in Fig. 7(b), the spectrum for $J_i = 0$ is dominated by the specular speak, whereas the intensity of this peak drastically decreases for $J_i = 3$. Note that small inaccuracies in the PES description may slightly influence the relative intensity of the diffraction peaks. In view of these results, we can conclude the following about the incident beam of H_2 molecules, of which the rotational state population is unknown due to its special formation mechanism: molecules with $J_i \neq 0$ would appear to be present in the beam, and they may well dominate its composition. Therefore, any attempt to reproduce experimental spectra along the [110] direction should consider rotationally excited molecules.

In Fig. 8, we have displayed the simulated spectra along the [100] and the [110] crystallographic directions, as a function of the wavelength associated with the projectile normal energy, for three initial rotational states, $J_i = 0$, 1, and 3. From this figure, we can see that along the [100] direction [see Fig. 8, panels (a), (b), and (c)] the shape of the diffraction spectrum does not depend significantly on J_i. Furthermore, the evolution of the spectra from the lower normal energies (the higher λ values) to the higher ones is rather smooth and the probability of the specular peak decreases, while the probability of the first order peaks increases slowly. For diffraction along the [110] direction [see Fig. 8, panels (d), (e), and (f)], the evolution of the spectra as a function of the normal energy is more complex. First, the shape of the spectrum depends strongly on the initial J_i values, the differences being more evident between $J_i = 0$ and $J_i > 0$. Second, the variation of the spectra with normal energy is far from being monotonous, especially for $J_i = 0$ [Fig. 8(d)]. From Fig. 8(d), it can be clearly seen that the first order peaks dominate the spectra for the lowest normal energies (the highest λ values). These peaks almost disappear when the energy (λ) increases (decreases), but for the highest energies considered here they become the dominant ones once again. A similar qualitative behavior is observed for the specular, second order, and third order peaks: they increase and decrease alternatively as a function of the incidence energy. In the case of rotationally excited molecules [Figs. 8(e) and 8(f)],

the diffraction spectra also show some structure, especially for the highest energies (the lowest λ's). Interestingly, by comparing Figs. 8(d), 8(e) and 8(f), we can infer that a combination of these spectra ($c_{J_0}P_{J_0} + c_{J_1}P_{J_1} + c_{J_2}P_{J_2}$) will yield results rather different from the individual ones, and will strongly depend on the weights (c_{J_0},c_{J_1},c_{J_2}). This fact reveals the need for further experimental developments aiming at characterizing the rotational distribution of the initial molecular beam.

Besides the different role played by the initial rotational state and the $V_{\rm els}$ potential for different incidence directions, one might wonder why the spectra for $J_i = 0$ along [100] and [110] directions [Figs. 8(a) and 8(d)] are so different, in view of the fact that $V_{\rm els} = 0$ in both cases. As already discussed in Ref. [14] for H/LiF(100), these differences can be understood in terms of the geometrical structure factor, S_g, which also modulates the intensity of diffraction peaks in polyatomic surfaces. S_g can be written as a function of the atomic form factor, f, as

$$S_g = f_{Li}e^{i\mathbf{G}\mathbf{d}_{Li}} + f_F e^{i\mathbf{G}\mathbf{d}_F}, \tag{14}$$

where $\mathbf{G}$ represent the reciprocal lattice $\mathbf{G} = m\mathbf{b}_1 + n\mathbf{b}_2$ and $d_{Li/F}$ the atomic basis set vectors. Thus S_g is equal to $f_{Li} + f_F$ if $n + m$ is even and $S_g = f_{Li} - f_F$ if $n + m$ is odd. For diffraction along [100], $n + m$ is always even, i.e., for all diffraction peaks $S_g = f_{Li} + f_F$, whereas, for diffraction along [110], $n + m$ is even and odd alternatively, i.e., S_g is equal to $f_{Li} + f_F$ and $f_{Li} - f_F$ for alternate diffraction peaks. Furthermore, the atomic form factors, f_{Li} and f_F, depend on the corrugation of the PES, which varies as a function of the crystallographic direction. Thus this mechanism may explain the stronger modulation obtained for diffraction along the [110] crystallographic direction [Fig. 8(d)]. Note that for another alkali-halide surface, such as KCl(100), the experimental diffraction patterns show the opposite behavior, i.e., the stronger modulation is observed for diffraction along the [100] direction [86].

To further analyze the role of $V_{\rm els}$ in the interaction of H_2 with LiF(001), we have also studied the variation of the diffraction spectra with incidence energy for different initial J_i and m_{J_i} values. As mentioned above, $V_{\rm els}$ depends on the molecule orientation through the coefficient $A_{n,m}(\theta,\phi)$; thus the influence of $V_{\rm els}$ should be different for molecules with different m_{J_i} values. In fact, from Fig. 9, where we display the diffraction spectra for $H_2(J_i = 3, m_{J_i} = 0, 1, 2, 3)$ along the [110] crystallographic direction, we can see that the spectrum is far more structured when the molecular bond lies parallel to the surface ($m_{J_i} = J_i$). This result further suggests that the interaction between the quadrupole moment of the molecule and the surface electric field depends on the orientation of the molecule. However, we should also take into account the geometrical structure factor, because the atomic form factors depend on the electronic density, i.e., on the corrugation of the PES, and the corrugation felt by a cartwheel molecule ($m_{J_i} = 0$) is, indeed, different from the one felt by a helicopter molecule ($m_{J_i} = J_i$). As already discussed in Ref. [54], the size of the ions is such that a neutral projectile would stay further away from F than from Li. Helicoptering H_2 molecules stay even further away from F, due to the repulsive interaction between the negative F ion and the excess of negative charge

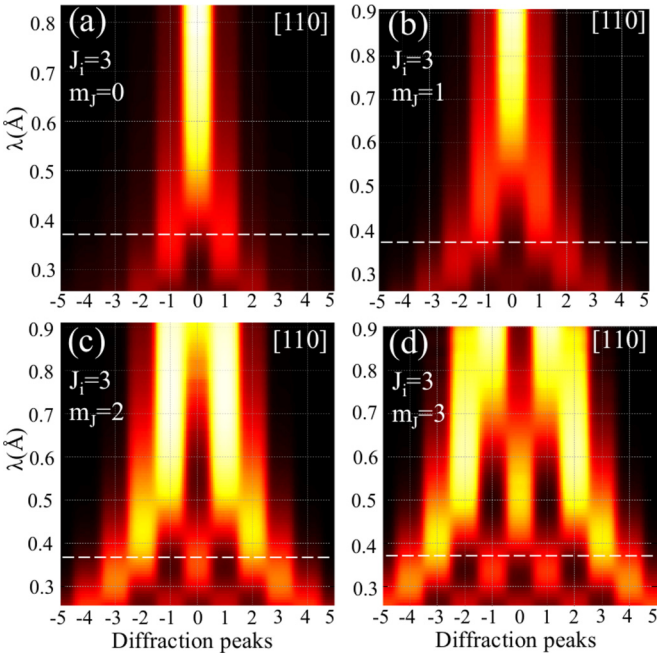

FIG. 9. 6D-TDWP theoretical simulated spectra for $H_2(J_i = 3, m_{J_i})$ diffracted from LiF(001), along the [110] crystallographic direction, as a function of the wavelength for motion normal to the surface. To take into account the experimental resolution our theoretical results have been convoluted by using a 2D Gaussian function with $\sigma_x = 0.4$ and $\sigma_y = 0.01$. The white dashed line indicates the wavelength associated to H_2 at 300 meV, the 1D cuts of which are shown in Fig. 7.

located in the H_2 bond, and get even closer to Li, due to the attractive interaction between the H_2 bond and the positive Li ion. The opposite is true for cartwheeling H_2 molecules, which see an almost flat surface. Therefore, we can consider both $V_{\rm els}$ and S_g responsible for the differences observed in the diffraction spectra as a function of m_J. At this point, it is worth mentioning that a similar analysis performed for diffraction along the [100] direction (results not shown here) does not show any significant difference for diffraction as a function of m_{J_i}. This is due, on the one hand, to the minor role that the quadrupole interaction plays for diffraction along this direction and, on the other hand, to the similar corrugation that helicopter and cartwheel molecules feel along this direction.

Finally, we have analyzed the probability of rotational inelastic diffraction. In Fig. 10, we show the total rotational excitation of H_2 upon scattering from LiF(001) as a function of the initial normal energy, for the three J_i states investigated here. From this figure, we can see that only molecules in the rotational ground state undergo a significant rotational excitation when the incidence normal energy increases, whereas the rotational excitation (or deexcitation) probability is rather small for H_2 ($J_i > 0$), much smaller for $J_i = 3$ than for $J_i = 1$. For example, the rotational excitation probability observed for $J_i = 1$, at the highest E_n investigated here, 572 meV, is 27% (23%) along the [110] ([100]) direction [Fig. 10(b)], whereas for $J_i = 3$ rotational excitation probability is lower than 10%, and rotational deexcitation lower than 15%, over the whole

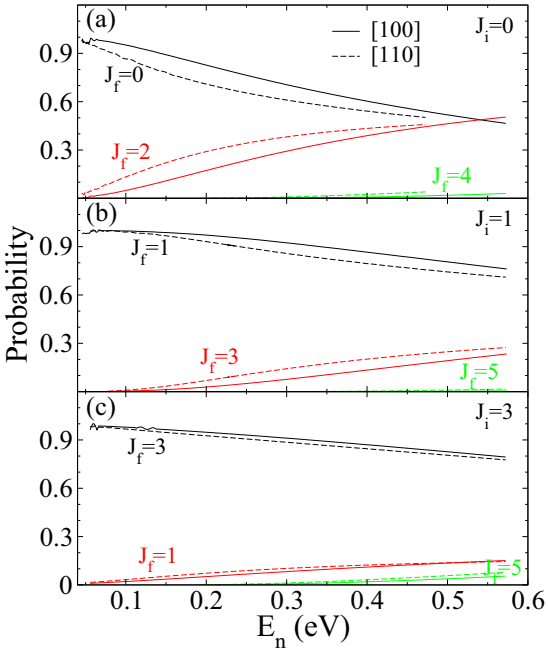

FIG. 10. Rotational excitation and deexcitation probabilities as a function of the normal incidence energy.

energy range [Fig. 10(c)]. In the light of these results, and taking into account that the experimental molecular beams are expected to contain a large amount of rotationally excited molecules, we can conclude that rotational inelastic diffraction does not play an important role, at least for normal incidence energies below 600 meV. This is an important advantage when analyzing experimental spectra, because due to the limitations of the experimental techniques, presently it is not possible to disentangle elastic from inelastic diffraction in GIFMD measurements.

IV. CONCLUSIONS

In this work, we have computed a six-dimensional (6D) potential energy surface (PES) for the H_2/LiF(001) system. This PES has been obtained by applying a modified version of the corrugation reducing procedure (CRP) to a set of density functional theory (DFT) energies. Based on this PES, we have performed quantum dynamics calculations, using both the time-dependent wave packet (TDWP) method and the multiconfiguration time-dependent Hartree (MCTDH) method. First, we have carried out simulations for low energy and normal incidence. From the good agreement between our results and previous results based on an analytical PES developed specifically for this system, we conclude that our DFT-based PES includes all the relevant physical effects responsible for the interaction of H_2 with LiF(001). And, by extension, that PESs obtained by applying the modified-CRP method to a set of DFT data set can be safely used to study the interaction of diatomic molecules with insulating surfaces.

In a second step, we have studied grazing incidence fast molecular diffraction (GIFMD) using both the TDWP and the MCTDH methods. From the good agreement between results obtained with these two methods, we can draw several conclusions. First, the close agreement between 5D and 6D wave packet results strongly suggests that the vibrational motion of H_2 only plays a minor role, and that it can be safely neglected. Second, grazing incidence conditions are reached for polar incidence angles higher than the ones usually used in experiment. The comparison between the simulated spectra and the experimental ones allows us to infer that most molecules present in the experimental molecular beam are rotationally excited, which means that the interaction between the quadrupole moment of the molecule and the electric field of the ionic surface ($V_{\rm els}$) plays a different role for the different crystallographic incidence directions.

Throughout this work, we have shown that more detailed information about the diffraction phenomenon, and therefore about the characteristics of the molecule/surface interaction, would be obtained by resolving the initial rotational state of the molecule, i.e., J_i and m_{J_i}. This is already possible in molecular beam diffraction experiments performed at thermal incidence energies [87–89]. We hope that the results presented in this work will stimulate similar developments in experimental methods used in GIFMD.

ACKNOWLEDGMENTS

Work supported by the MINECO projects No. FIS2013-42002-R, No. FIS2016-77889-R, and No. CTQ2013-50150-EXP, CAM Project NANOFRONTMAG No. S2013/MIT-2850, and the European Research Council through an ERC-2013 advanced Grant No. 338580. M.d.C. and A.S.M. acknowledge the FPI program of the MINECO co-financed by the European Social Fund. C.D. acknowledges the Ramón y Cajal program of the MINECO. We acknowledge computer time provided by the Centro de Computación Científica of the Universidad Autónoma de Madrid and the Red Española de Supercomputación.

[1] A. Schuller, S. Wethekam, and H. Winter, Phys. Rev. Lett. **98**, 016103 (2007).
[2] P. Rousseau, H. Khemliche, A. G. Borisov, and P. Roncin, Phys. Rev. Lett. **98**, 016104 (2007).
[3] H. Winter and A. Schuller, Prog. Surf. Sci. **86**, 169 (2011).
[4] J. Seifert, A. Schuller, H. Winter, R. Wlodarczyk, J. Sauer, and M. Sierka, Phys. Rev. B **82**, 035436 (2010).
[5] J. Seifert, M. Busch, E. Meyer, and H. Winter, Phys. Rev. B **89**, 075404 (2014).
[6] A. Schuller, H. Winter, M. S. Gravielle, J. M. Pruneda, and J. E. Miraglia, Phys. Rev. A **80**, 062903 (2009).
[7] H. Winter (private communication).
[8] M. S. Gravielle and J. E. Miraglia, Phys. Rev. A **78**, 022901 (2008).
[9] A. Ruiz, J. P. Palao, and E. J. Heller, Phys. Rev. A **79**, 052901 (2009).
[10] M. S. Gravielle, G. A. Bocan, and R. Díez Muiño, Phys. Rev. A **82**, 052904 (2010).

[11] P. Tiwald, A. Schuller, H. Winter, K. Tokesi, F. Aigner, S. Grafe, C. Lemell, and J. Burgdorfer, Phys. Rev. B **82**, 125453 (2010).
[12] A. Schuller, D. Blauth, J. Seifert, M. Busch, H. Winter, K. Gartner, R. Wlodarczyk, and J. Sauer, Surf. Sci. **606**, 161 (2012).
[13] C. A. R. Rubiano, G. A. Bocan, M. S. Gravielle, N. Bundaleski, H. Khemliche, and P. Roncin, Phys. Rev. A **87**, 012903 (2013).
[14] A. S. Muzas, F. Martín, and C. Díaz, Nucl. Instrum. Methods, B **354**, 9 (2015).
[15] M. Debiossac, A. Zugarramurdi, H. Khemliche, P. Roncin, A. G. Borisov, A. Momeni, P. Atkinson, M. Eddrief, F. Finocchi, and V. H. Etgens, Phys. Rev. B **90**, 155308 (2014).
[16] A. S. Muzas, F. Gatti, F. Martín, and C. Díaz, Nucl. Instrum. Methods, B **382**, 49 (2016).
[17] U. van Slooten, E. J. J. Kirchner, and A. W. Kleyn, Surf. Sci. **283**, 27 (1993).
[18] U. van Slooten and A. W. Kleyn, Chem. Phys. **177**, 509 (1993).
[19] C. Díaz, P. Rivière, and F. Martín, Phys. Rev. Lett. **103**, 013201 (2009).
[20] A. Gross, Surf. Sci. Rep. **32**, 291 (1998).
[21] G. J. Kroes, Prog. Surf. Sci. **60**, 1 (1999).
[22] G. J. Kroes and M. F. Somers, J. Theor. Comput. Chem. **04**, 493 (2005).
[23] C. Díaz, E. Pijper, R. A. Olsen, H. F. Busnengo, D. J. Auerbach, and G. J. Kroes, Science **326**, 832 (2009).
[24] G. J. Kroes and C. Díaz, Chem. Soc. Rev. **45**, 3658 (2016).
[25] D. Farías, C. Díaz, P. Rivière, H. F. Busnengo, P. Nieto, M. F. Somers, G. J. Kroes, A. Salin, and F. Martín, Phys. Rev. Lett. **93**, 246104 (2004).
[26] P. Nieto, E. Pijper, D. Barredo, G. Laurent, R. A. Olsen, E. J. Baerends, G. J. Kroes, and D. Farías, Science **312**, 86 (2006).
[27] M. Wijzenbroek and G. J. Kroes, J. Chem. Phys. **140**, 084702 (2014).
[28] H. F. Busnengo, A. Salin, and W. Dong, J. Chem. Phys. **112**, 7641 (2000).
[29] C. Crespos, M. A. Collins, E. Pijper, and G. J. Kroes, Chem. Phys. Lett. **376**, 566 (2003).
[30] T. J. Frankcombe, C. M. Collins, and D. H. Zhang, J. Chem. Phys. **137**, 144701 (2012).
[31] S. Lorenz, A. Gross, and M. Scheffler, Chem. Phys. Lett. **395**, 210 (2004).
[32] K. Shakouri, J. Behler, J. Meyer, and G. J. Kroes, J. Phys. Chem. Lett. **8**, 2131 (2017).
[33] B. Jiang and H. Guo, J. Chem. Phys. **141**, 034109 (2014).
[34] X. J. Shen, Y. Xiao, W. Dong, X. H. Yan, and H. F. Busnengo, Comput. Theor. Chem. **990**, 152 (2012).
[35] P. Rousseau, H. Klemliche, N. Bundaleski, P. Soulisse, A. Momeni, and P. Roncin, J. Phys.: Conf. Ser. **133**, 012013 (2008).
[36] I. Estermann and O. Stern, Z. Phys. **61**, 95 (1930).
[37] R. Frisch and O. Stern, Z. Phys. **84**, 430 (1933).
[38] J. E. Lennard-Jones and A. F. Devonshire, Nature (London) **137**, 1069 (1936).
[39] G. Boato, P. Cantini, and L. Mattera, J. Chem. Phys. **65**, 544 (1976).
[40] R. Horne and L. J. F. Hermans, J. Chem. Phys. **91**, 1261 (1989).
[41] W. Allison and B. Feuerbacher, Phys. Rev. Lett. **45**, 2040 (1980).
[42] G. Wolken, J. Chem. Phys. **59**, 1159 (1973).
[43] G. Wolken, J. Chem. Phys. **68**, 4338 (1978).
[44] G. Wolken, J. Chem. Phys. **62**, 2730 (1975).
[45] L. M. Hubbard and W. H. Miller, J. Phys. Chem. **78**, 1801 (1983).
[46] R. B. Gerber, A. T. Yinnon, Y. Shimoni, and D. J. Kouri, J. Chem. Phys. **73**, 4397 (1980).
[47] G. Drolshagen, A. Kaufhold, and J. P. Toennies, J. Chem. Phys. **83**, 827 (1985).
[48] U. Garibaldi, A. C. Levi, R. Spadicini, and G. E. Tommei, Surf. Sci. **55**, 40 (1976).
[49] T. R. Proctor, D. J. Kauri, and R. B. Gerber, J. Chem. Phys. **80**, 3845 (1984).
[50] J. V. Lill and D. J. Kauri, Chem. Phys. Lett. **112**, 249 (1984).
[51] R. C. Mowrey and D. J. Kouri, J. Chem. Phys. **84**, 6466 (1986).
[52] A. V. Levi and V. Tarditi, Surf. Sci. **235**, 1989 (1989).
[53] N. R. Hill, Phys. Rev. B **19**, 4269 (1979).
[54] G. J. Kroes and R. C. Mowrey, J. Chem. Phys. **103**, 2186 (1995).
[55] E. Pijper and G. J. Kroes, Phys. Rev. Lett. **80**, 488 (1998).
[56] M. F. Bertino, A. L. Glebov, J. P. Toennies, F. Traeger, E. Pijper, G. J. Kroes, and R. C. Mowrey, Phys. Rev. Lett. **81**, 5608 (1998).
[57] Y. Ekinci and J. P. Toennies, Phys. Rev. B **72**, 205430 (2005).
[58] R. Valero, G. J. Kroes, Y. Ekinci, and J. P. Toennies, J. Chem. Phys. **124**, 234707 (2006).
[59] M. H. Beck, A. Jäckle, G. A. Worth, and H. D. Meyer, Phys. Rep. **324**, 1 (2000).
[60] M. del Cueto, A. S. Muzas, M. F. Somers, G. J. Kroes, C. Díaz, and F. Martín, Phys. Chem. Chem. Phys. **19**, 16317 (2017).
[61] G. Laurent, D. Barredo, D. Farías, R. Miranda, C. Díaz, P. Rivière, M. F. Somers, and F. Martín, Phys. Chem. Chem. Phys. **12**, 14501 (2010).
[62] J. Lienemann, A. Schuller, D. Blauth, J. Seifert, S. Wethekam, M. Busch, K. Maass, and H. Winter, Phys. Rev. Lett. **106**, 067602 (2011).
[63] G. Kresse and J. Furthmuller, Phys. Rev. B **54**, 11169 (1996).
[64] G. Kresse and D. Joubert, Phys. Rev. B **59**, 1758 (1999).
[65] J. P. Perdew, J. A. Chevary, S. H. Vosko, K. A. Jackson, M. R. Pederson, D. J. Singh, and C. Fiolhais, Phys. Rev. B **46**, 6671 (1992).
[66] P. E. Blöchl, Phys. Rev. B **50**, 17953 (1994).
[67] A. Schüller, S. Wethekam, D. Blauth, H. Winter, F. Aigner, N. Simonovic, B. Solleder, J. Burgdörfer, and L. Wirtz, Phys. Rev. A **82**, 062902 (2010).
[68] N. A. Smirnov, Phys. Rev. B **83**, 014109 (2011).
[69] J. Liu, L. Dubrovinsky, T. B. Ballaran, and W. Crichton, High Press. Res. **27**, 483 (2007).
[70] F. W. de Wette, W. Kress, and U. Schröder, Phys. Rev. B **32**, 4143 (1985).
[71] N. P. Wang, M. Rohlfing, P. Krüger, and J. Pollmann, Phys. Rev. B **67**, 115111 (2003).
[72] R. Kosloff, J. Phys. Chem. **92**, 2087 (1988).
[73] H. D. Meyer and G. A. Worth, Theor. Chem. Acc. **109**, 251 (2003).
[74] J. C. Light, I. P. Hamilton, and J. V. Lill, J. Chem. Phys. **82**, 1400 (1985).
[75] G. C. Corey and D. Lemoine, J. Chem. Phys. **97**, 4115 (1992).
[76] M. D. Feit, J. J. A. Fleck, and A. Steiger, J. Comput. Phys. **47**, 412 (1982).
[77] R. C. Mowrey and G. J. Kroes, J. Phys. Chem. **103**, 1216 (1995).
[78] G. G. Balint-Kurti, R. N. Dixon, and C. C. Marston, J. Chem. Soc. Faraday Trans. **86**, 1741 (1990).
[79] G. G. Balint-Kurti, R. N. Dixon, and C. C. Marston, Int. Rev. Phys. Chem. **11**, 317 (1992).

[80] E. Pijper, G. J. Kroes, R. A. Olsen, and E. J. Baerends, J. Chem. Phys. **117**, 5885 (2002).
[81] M. H. Beck, G. A. Worth, A. Jäckle, and H. D. Meyer, The MCTDH Package, Version 8.5, http://mctdh.uni-hd.de/.
[82] A. Jäckle and H. D. Meyer, J. Chem. Phys. **104**, 7974 (1996).
[83] A. Jäckle and H. D. Meyer, J. Chem. Phys. **109**, 3772 (1998).
[84] G. J. Kroes and R. C. Mowrey, Chem. Phys. Lett. **232**, 258 (1995).
[85] D. Farías, C. Díaz, P. Nieto, A. Salin, and F. Martín, Chem. Phys. Lett. **390**, 250 (2004).
[86] E. Meyer, Ph.D. thesis, Humboldt-Universität zu Berlin, 2015, https://edoc.hu-berlin.de/handle/18452/18094.
[87] L. C. Shackman and G. O. Sitz, J. Chem. Phys. **123**, 064712 (2001).
[88] E. Watts and G. O. Sitz, J. Chem. Phys. **114**, 4171 (2001).
[89] O. Godsi, G. Corem, Y. Alkoby, J. T. Cantin, R. V. Krems, M. F. Somers, J. Meyer, G. J. Kroes, T. Maniv, and G. Alexandrowicz, Nat. Commun. **8**, 15357 (2017).